Earth and Planetary Science Letters 288 (2009) 370–381

Contents lists available at ScienceDirect

Earth and Planetary Science Letters

journal homepage: www.elsevier.com/locate/epsl

Self-similarity of the largest-scale segmentation of the faults: Implications for earthquake behavior

Isabelle Manighetti *, Dimitri Zigone, Michel Campillo, Fabrice Cotton

Laboratoire de Géophysique Interne et Tectonophysique (LGIT), CNRS, Observatoire de Grenoble (OSUG), Université J. Fourier, Maison des Géosciences, BP 53, 38041 Grenoble cédex 09, France

ARTICLE INFO

Article history:
Received 25 June 2009
Received in revised form 25 September 2009
Accepted 26 September 2009
Available online 25 October 2009

Editor: R.D. van der Hilst

Keywords:
fault segmentation
earthquakes
fault
earthquake mechanics

ABSTRACT

Earthquakes are sensitive to the along-strike segmentation of the faults they break, especially in their initiation, propagation and arrest. We examine that segmentation and search whether it shows any specific properties. We focus on the largest-scale fault segmentation which controls the largest earthquakes. It is well established that major segments within faults markedly shape their surface cumulative slip-length profiles; segments appear as large slip bumps separated by narrow, pronounced slip troughs (inter-segments). We use that property to examine the distribution (location, number, length) of the major segments in 927 active normal faults in Afar (East Africa) of various lengths (0.3–65 km), cumulative slips (1–1300 m), slip rates (0.5–5 mm/yr), and ages (10^4–10^6 yr). This is the largest fault population ever analyzed. To identify the major bumps in the slip profiles and determine their number, location and length, we analyze the profiles using both the classical Fourier transform and a space–frequency representation of the profiles, the S-transform, which is well adapted for characterizing local spectral properties. Our work reveals the following results: irrespective of their length, 70% of the slip profiles have a triangular envelope shape, in conflict with the elastic crack concept. Irrespective of their length, the majority of the faults (at least 50–70%) have a limited number of major segments, between 2 and 5 and more commonly equal to 3–5. The largest-scale segmentation of the faults is thus self-similar and likely to be controlled by the fault mechanics. The slip deficits at the major inter-segment slip troughs tend to smooth as the faults accumulate more slip resulting in increased connection of the major segments. The faults having accumulated more slip therefore generally appear as un-segmented (10–30%). Our observations therefore show that, whatever the fault on which they initiate, large earthquakes face the same number of major segments to potentially break. The number of segments that they eventually break seems to depend on the slip history (structural maturity) of the fault.

1. Introduction

It is long known that faults are segmented, that is, even though they overall appear as planar continuous structures of finite length, faults are in fact irregular, nonplanar surfaces consisting of a number of discrete planar subparallel segments separated by geometrical discontinuities referred to as 'inter-segments' (Fig. 1) (e.g., Tchalenko and Berberian, 1975; Segall and Pollard, 1980; Sibson, 1986; Barka and Kandisky-Cade, 1988; Aydin and Schultz, 1990; Scholz et al., 1991; Peacock, 1991; Ferrill et al., 1999; Zhang et al., 1999; Walsh et al., 2003; Soliva and Benedicto, 2004). The segments may be connected along the surface fault trace, which, in that case, shows marked deflections (bends) at the inter-segments (Figs. A1 and A8 in Electronic Supplement). Conversely, the segments may appear disconnected at the surface, being laterally offset along the fault trace (Figs. 1 and A8 in Electronic Supplement). The across-strike separation between the segments is small however (ratio to fault length of 10^{-1}–10^{-2}, Fig. 1), indicating that the segments are mechanically linked, hence are 'constitutive ingredients' of a larger-scale fault, not independent small faults. The segmentation is present for all scales and slip modes of faults. Besides segments within faults span a broad range of scales (e.g., Tchalenko and Berberian, 1975; Segall and Pollard, 1980; Aydin and Schultz, 1990; Scholz et al., 1991), so that the fault traces appear punctuated by a number of geometrical discontinuities of various sizes. It has been argued that the resulting overall fault structure is fractal (e.g., Brown and Scholz, 1985; Okubo and Aki, 1987; Power et al., 1987; Kagan, 1994). A number of studies have also suggested that the segmentation of the faults is controlled by the stratigraphic and material properties of the faulted medium (Aviles and Scholz, 1987; Scholz et al., 1991), with the seismogenic thickness dictating the length of the major segments within faults (e.g., Sylvester, 1988; Jackson, 2002; Walsh et al., 2003; Klinger et al., 2006). It is uncertain whether all segments identified in the surface fault traces persist at crustal depth, but a number of seismological and geophysical studies demonstrate that at least the largest segmentation of the faults is a 3D property (e.g., Simpson et al., 2006; Li et al., 1994).

* Corresponding author.
E-mail address: imanighe@obs.ujf-grenoble.fr (I. Manighetti).

0012-821X/$ – see front matter © 2009 Elsevier B.V. All rights reserved.
doi:10.1016/j.epsl.2009.09.040

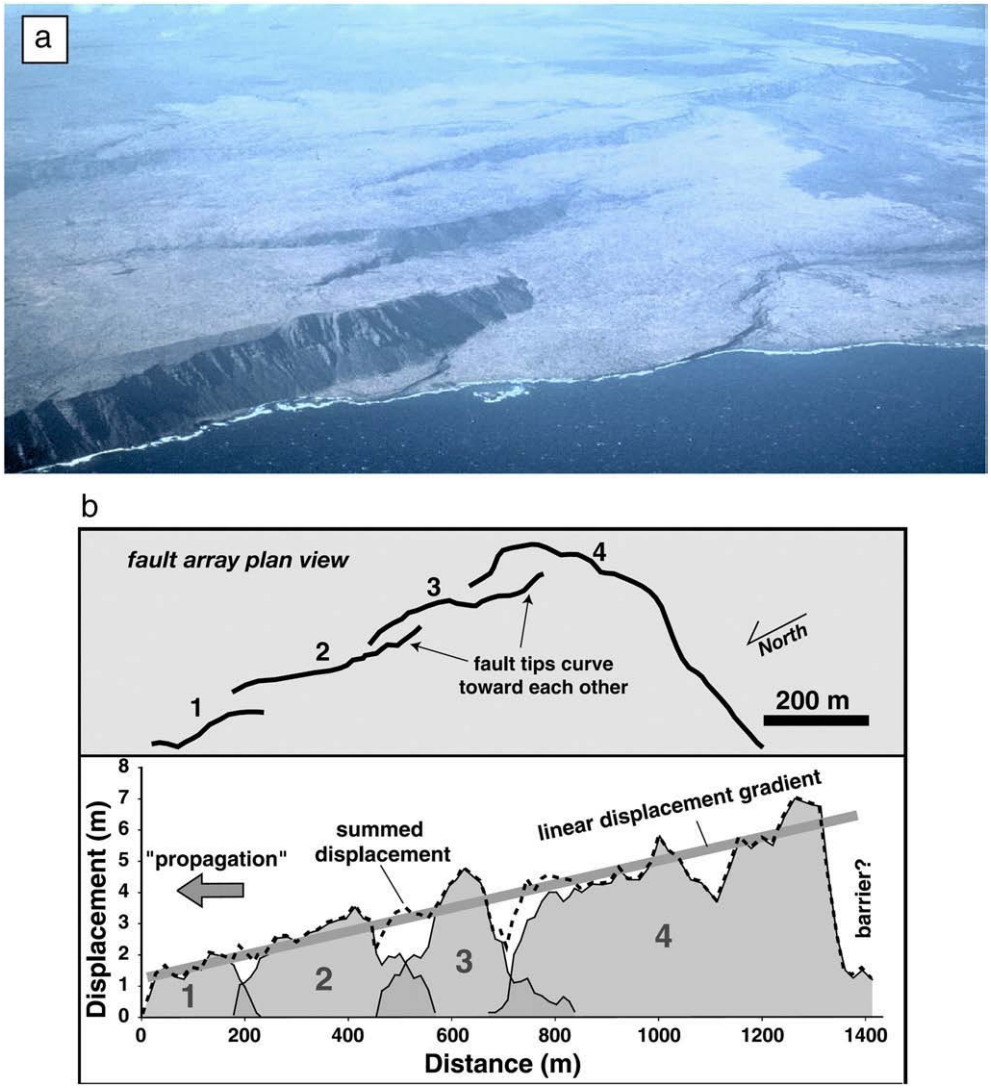

Fig. 1. Examples of segmented faults worldwide. a) En echelon segmented Hilina normal fault, Hawaii (from http://volcano-pictures.info/glossary/fault.html). b) Top, surface trace of the Glastone reverse fault clearly made of 4 major segments (from Davis et al., 2005); bottom, cumulative slip-length profile of the Glastone fault, showing the clear signature of the major segments and inter-segments.

Large earthquakes ($M>6$) corroborate the hypothesis of deep rooted major segments as most large ruptures are clearly controlled by the major geometrical complexities of the faults on which they occur (e.g., Segall and Pollard, 1980; Sibson, 1985; King and Nabelek, 1985; Manighetti et al., 2005; Wesnousky, 2008). Firstly, it is observed that most large faults do not rupture along their entire length during an earthquake, but instead break only along one or a few of their segments (e.g., Schwartz and Coppersmith, 1984; dePolo et al., 1991; Machette et al., 1991; Zhang et al., 1991, 1999), sometimes in a cascade-like fashion (e.g., Manighetti et al., 2007; Shaw and Dieterich, 2007). As many sizes of earthquakes occur on a given fault, many sizes of segments are obviously involved in the fault ruptures. Secondly, it is also observed that most earthquake ruptures stop at geometrical discontinuities along faults, mainly steps between segments and termini of fault traces (Schwartz and Coppersmith, 1984; Sibson, 1985; King and Nabelek, 1985; Barka and Kandisky-Cade, 1988; Harris and Day, 1993; Lettis et al., 2002; Das, 2003; Manighetti et al., 2005; Wesnousky, 2006, 2008). As the earthquake size increases, the size (i.e., across-fault strike width) of the inter-segments required to potentially arrest the rupture seems to increase accordingly, up to a ≈5 km threshold (e.g., Harris and Day, 1993; Stirling et al., 1996; Harris and Day, 1999; Zhang et al., 1999; Wesnousky, 2006).

The 'structural, lateral properties' of the long-term geological faults, i.e., the way they are segmented along their length, thus is a controlling factor in the earthquake process. Characterizing the segmentation of the faults, that is finding an objective, quantitative manner to describe it, is therefore a key issue for anyone concerned with earthquake and fault mechanics and with seismic hazard. We address this question by focusing on the largest-scale segmentation of the faults, as it potentially controls the largest, most threatening earthquakes. We are thus concerned here with the longest segments within faults, whose length is of magnitude of that of the fault they belong to. Those longest segments are expected to be 3D features, extending from surface to seismogenic depths. The question that we specifically address is whether the large-scale segmentation of the faults exhibits any systematic pattern that could be quantitatively described.

The few studies that have been carried out so far on fault segmentation have identified the fault segments from their specific expression along the surface fault traces (e.g., Stirling et al., 1996). Most fault traces commonly appear as arrays of more or less connected echelon segments (Fig. 1), so that mapping the distribution of bends and offsets along a main fault trace may allow identifying and discriminating the various-scales segments that form the fault. Yet identifying bends, offsets and any other sorts of geometrical discontinuities along fault

traces is not everywhere straightforward and requires accurate fault maps that actually only exist at present for a limited number of faults. Those caveats make difficult to use the fault trace geometry only to search for general properties of the fault segmentation. For those reasons we here follow a different, new approach. An interesting property of the long-term faults is that their cumulative slip-length profiles, which depict the variation of the long-term slip as a function of the entire fault length, retain in their shaping important information on the major segments that form the faults (Fig. 1b). More specifically, major segments along faults form large slip bumps in their total slip-length profile, separated by pronounced narrow slip troughs which coincide with the inter-segment discontinuities (e.g., Ellis and Dunlap, 1988; Peacock and Sanderson, 1991; Peacock, 1991; Manighetti et al., 2001a; Walsh et al., 2003; Soliva and Benedicto, 2004; Davis et al., 2005). Such a shaping of the slip profiles into bumps and troughs results from most of the slip being accommodated along the discrete fault segments, while the discontinuities that separate them act as long-lived, hardly slipping transfer zones. The coincidence in location of the major slip troughs identified in a coseismic slip profile and of the major inter-segments of the broken fault, confirms that the major inter-segment zones act as long-lived, persisting barriers to slip propagation (Fig. A2 in Electronic Supplement).

Pronounced fluctuations in cumulative slip profiles thus hold information on the location, size and number of the major segments that constitute the faults. Cumulative slip profiles can however only be measured on dip-slip faults, especially normal faults, as slip-recording markers are absent along most of the length of strike-slip faults. We consequently analyze cumulative slip profiles on a population of active normal faults (Afar, East Africa). As we intend to examine whether the large-scale segmentation of the faults has any systematic, robust, scale-invariant property, we analyze an extremely dense population of slip profiles (927) spanning a broad range of length scales (fault lengths: 1–10^2 km). This is actually the largest fault population ever analyzed so far.

In the following, we use two different signal-processing methods — Fourier Spectrum and S-transform — to recover the number and size of the largest bumps in each of the 927 slip profiles, which we use as a proxy for major segments. We find that, irrespective of their scale, the vast majority of faults have 2–5, and more commonly 3–5, major segments. This result places important bounds on the maximum length that an earthquake rupture can break on a specific fault.

2. Data sets

The normal fault population that we analyze is that currently dissecting the desertic Afar, East Africa region (Fig. 2). It is the same fault population and the same data set, though greatly expanded (927 faults analyzed here versus 255 in the previous analysis), as those previously described in detail by Manighetti et al. (2001a), in their analysis of the generic properties of the fault cumulative slip-length profiles. We here only recall the main characteristics of the faults and slip data, while further detail can be found in Manighetti et al. (2001a).

All the faults that we analyze have been identified and mapped in prior studies (Manighetti et al., 1997, 1998, 2001a,b; Audin et al., 2001), while their cumulative slip-length profiles were measured previously by the first author. Note that each analyzed fault has a continuous surface trace. The faults studied offset the basalt surface of Afar, 95% on land and 5% in shallow water. All form clear escarpments in the topography and bathymetry, which have been shown to provide well-preserved records of the cumulative vertical slip along the faults. The cumulative slip-length profiles were originally extracted from three high-resolution digital elevation models (DEMs), following the method described in Manighetti et al. (2001a).

14% of the faults that we analyze are located within the Asal–Ghoubbet rift (Fig. 2b, 81 faults in the on land part of the rift, and 47 in its underwater section; e.g., Manighetti et al., 1998), while the rest of the faults are offsetting the large regions of Afar that extend outside and in between the numerous rift segments (Fig. 2a; Manighetti et al., 2001b). Slip profiles on the Asal–Ghoubbet faults were extracted from two DEMs with a pixel size of ≈15 m and an elevation accuracy of ±1 m (e.g. De Chabalier and Avouac, 1994; Audin et al., 2001). Maximum uncertainties on slip and length measurements for those faults have been estimated to be ±3 and 50 m, respectively (Manighetti et al., 2001a). Slip profiles on the other Afar faults were extracted from the worldwide SRTM DEM, whose pixel size is 90 m and elevation accuracy ±20 m. Maximum uncertainties on slip and length measurements for those 'Afar faults' have been estimated to be ±25 and 400 m, respectively (Manighetti et al., 2001a).

A total of 1927 slip profiles were originally extracted. From that extremely dense dataset, we only retain here the faults whose maximum slip is at least three times greater than the error on the vertical measurements. This results in a final population of 927 faults, the largest fault population ever analyzed so far. Those faults span a broad range of lengths (0.3–65 km, Fig. 3a) and maximum slips (3–1300 m, Fig. 3b). When the fault lengths are expressed as a function of the seismogenic thickness (W_{seism}) which they cut through (≈5 km in Asal–Ghoubbet and ≈10 km elsewhere; e.g., Doubre et al., 2007a,b; Manighetti et al., 2001b; Fig. 3c), the fault population appears to span a broad range of scales, with lengths varying from being much smaller (53% of the faults have a length shorter than W_{seism}) to much larger (up to $6\times W_{seism}$) than the thickness of the crust. The fault ages also vary, between about 10^4 and 10^6 yr, while their slip rates range between 0.5 and 5 mm/yr (e.g., Stein et al., 1991; Manighetti et al., 1998, 2001a,b). Thus, not only the fault population that we analyze is extremely dense, but it also spans a broad range of sizes, ages and slip rates, making it possible to search for scale-invariant properties.

3. Data analysis

The vast majority of the profiles contain hundreds of data points. Prior to analysis, we slightly smoothed them (running average over 4 points) in order to minimize the extremely high frequencies (generally >50–100) related to noise in the measurements. Fig. 4 shows 8 out of the 927 analyzed slip profiles. We will refer to those examples at all steps of our analysis, to better highlight the different methods that we apply to the entire fault population. The examples have been chosen to span different fault sizes (1–60 km), slips (14–420 m), ages (10^4–10^6 yr) and locations (details in caption).

Regardless of the difference in these parameters for the chosen examples, they all have a bumpy shape. On each fault, the distribution of slip along the fault length appears as a fluctuating signal, dominated by large bumps separated by narrower slip troughs. A visual counting of the largest bumps suggests that the example faults include at most 2–5 of such major bumps (numbers reported on figure). Fig. A1 in Electronic Supplement shows the surface traces of two of the example faults, and confirms that the major bumps visually identified in the slip profiles coincide with major segments along the fault traces.

Our aim is to determine the number of major slip bumps, hence major segments, along each of the 927 slip profiles. Visual observation and counting is not the easiest procedure to analyze such a dense dataset. We therefore chose to analyze the slip profiles using methods aimed at quantitatively describing the spectral energy content of the fluctuating slip signals. Because the slip profiles are far from being stationary, a classical Fourier spectrum approach is not fully appropriate. We therefore also use a space–frequency representation of the slip profiles, namely the S-transform, to characterize local spectral properties.

3.1. Envelope shape of the slip profiles

Slip bumps and troughs are defined with respect to the overall envelope shape of the slip profiles; they can be considered to be fluctuations around the function that best averages the overall slip

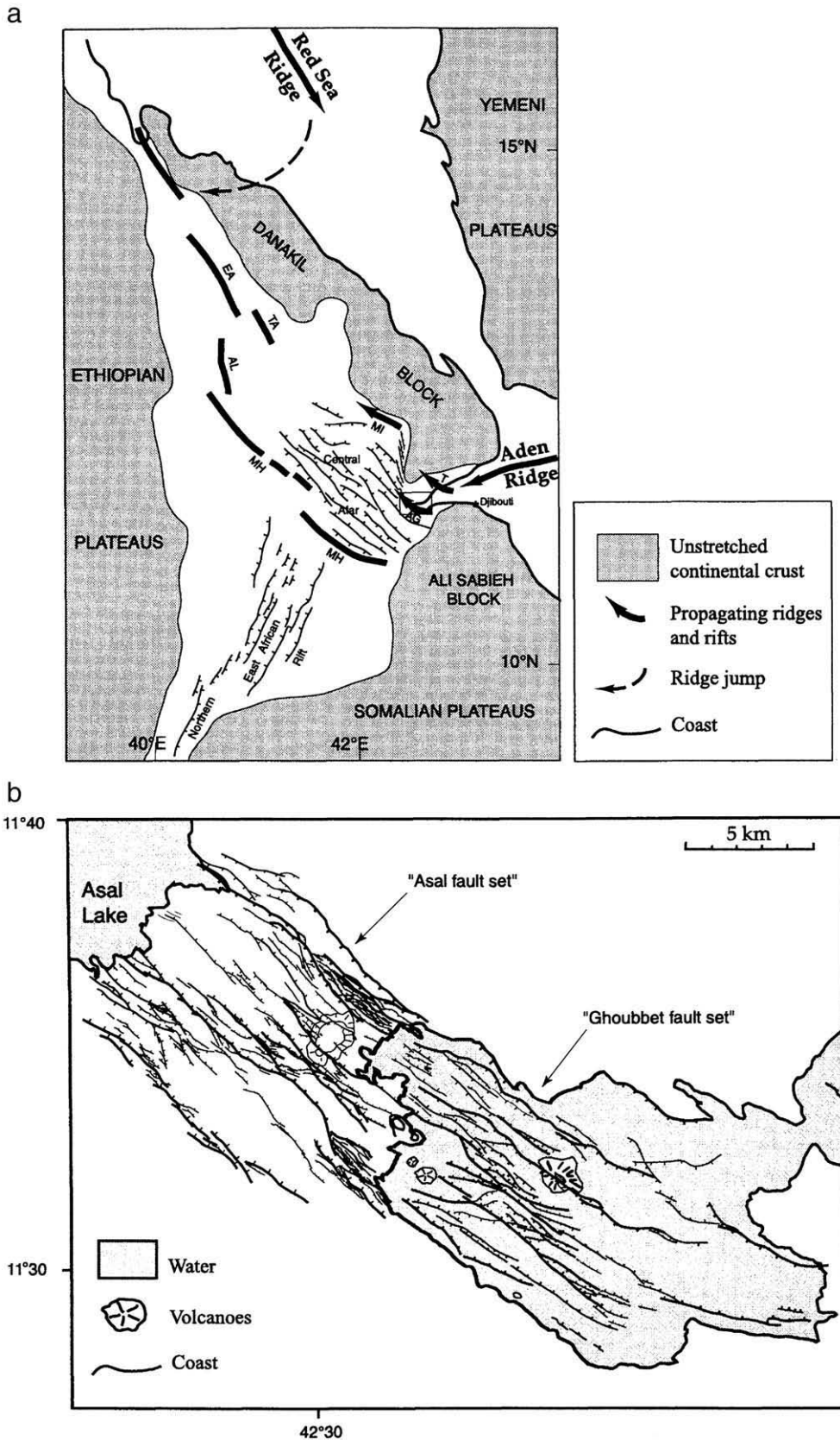

Fig. 2. Tectonic setting of the analyzed Afar normal faults. a) Major faults in central Afar (from Manighetti et al., 2001b), most are referred to as S_{fault} in the text. b) Major faults in Asal–Ghoubbet rift (from Manighetti et al., 1998, 2001a), referred to as A_{fault} and G_{fault} in the text.

distribution. The first step of the analysis is therefore to estimate the envelope shape of the 927 slip profiles and find the function(s) that best approximates them.

A visual inspection of the slip profiles reveals that most of them exhibit an overall triangular shape, generally asymmetric (examples a–f in Fig. 4), while the other few profiles more resemble an elliptical

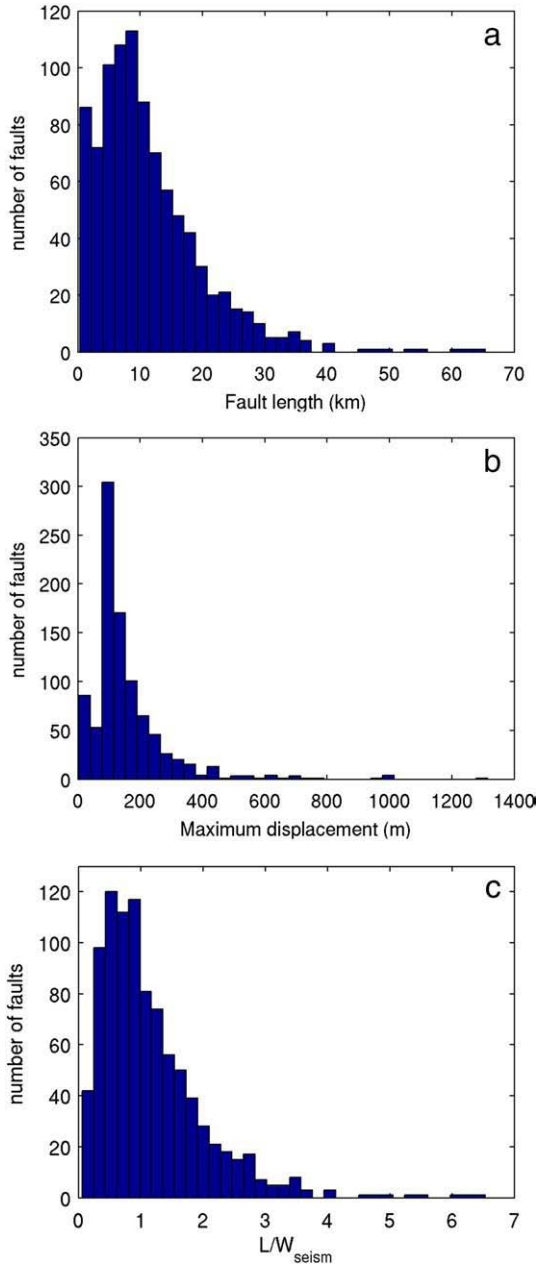

Fig. 3. Statistics of the analyzed fault population. a) Distribution of fault lengths. b) Distribution of maximum displacements on the faults. c) Distribution of fault lengths expressed as a function of the seismogenic crust thickness (W_{seism}).

function (examples g–h in Fig. 4). Those findings are similar to the observations reported by Manighetti et al. (2001a). Though a triangular shape is not expected from the elastic crack theory commonly used to describe faults (e.g., Scholz, 2002), it has been recently shown to be actually the shape most commonly characterizing the slip-length distributions on both faults (e.g., Manighetti et al., 2001a; Scholz, 2002; Davis et al., 2005; Nicol et al., 2005) and earthquake ruptures (Manighetti et al., 2005; Wesnousky, 2008). This shows that the triangular distribution of slip as a function of length is a robust, scale-invariant property of faults.

To check whether our slip profiles are best approximated by a triangular or an elliptical function, we use a least squares method to determine, for each profile, the triangle and the ellipse that best-fit the data (minimum RMS value), subsequently choosing the final best-fitting function as the best of the two (blue dotted curves in Fig. 4).

Applied to the entire population of the 927 slip profiles, the above analysis reveals that 70% of the profiles are best fitted by a triangular shape (asymmetric for ≈74% of that 'triangular population', with asymmetry defined when best-fitting maximum slip is beyond 10% of L from fault center), while the rest of the profiles are more satisfactorily approximated by an elliptical function. This confirms that the triangular distribution of slip is an intrinsic, self-similar property of the faults, with a robust physical meaning (as also has the elliptical function; see detailed discussions in Manighetti et al., 2001a, 2005). The total slip function of a fault (function T) can therefore be viewed as the sum of two functions, one (triangular or elliptical) that describes the average distribution of slip (function G), and another one that describes the slip fluctuations which result from the fault segmentation (function $f = T - G$).

The aim of this study being to characterize the fluctuating part of the slip signals, that is the function f, we first isolate it by removing the best-fitting envelope shape (G) from the measured slip profiles (T), for each of the 927 faults. The analyses described below are conducted on those 'residual' T–G parts of the slip profiles (as represented in Fig. 5).

Note that, before being analyzed, the slip profiles are normalized to both their length and maximum slip. Any 'specific length scale' described below is thus only a relative value.

3.2. Fourier spectrum analysis of the slip profiles

The Fourier spectrum is certainly the simplest and most common characterization of a fluctuating signal. That spectrum represents the contribution over the total signal of sinusoids of different spatial frequencies, which are thus inverse of length scales. Yet, though the method allows quantifying the contributions of different length scales over the total signal, it abuts a major limitation: because the sinusoids are not localized, only average contributions over the whole profile can be determined. Thus the method cannot account easily for isolated slip fluctuations, nor describe the possible spatial variability in the fluctuation lengths.

Fig. 5 shows the Fourier spectrum obtained for the 8 example slip profiles. The histograms report the mean amplitude of the frequency components as a function of the spatial frequency. A spatial frequency equal to N means that the Fourier wavelength is L/N, with L the fault length. We only examine a low frequency range (1–8) since we are concerned with largest slip fluctuations only. Remember that, as said before, the analysis is conducted on the fluctuating parts of the slip signals (f) (middle plots in Fig. 5). The amplitude at zero frequency is the average of the function f. Dominance of this frequency in the spectrum means that the residual function f is better represented by its overall mean than by a series of sinusoids.

The histograms show that, in all examples, the greatest signal energy occurs over a narrow range of spatial frequencies. This shows that each slip signal is quite well described by sinusoids having spatial frequencies in a narrow and specific range. Those specific frequency ranges are in all cases greater than 1, what confirms that all example slip profiles contain significant oscillations. Those oscillations have a specific spatial frequency range, hence a specific relative length scale. Finally, we note that the numbers of major slip bumps that are derived from the dominant spatial frequencies are similar to the numbers of major slip bumps as determined before from visual observation (Fig. 4).

Together these suggest that we may apply the Fourier spectrum analysis to the entire data set to recover the number and average relative size of the major slip bumps which most dominate the slip-length profiles. The width of the spectra makes it difficult to visualize all the spectra in a single plot. We therefore extracted the dominant frequencies, for each fault, i.e. the frequencies for which the amplitude is higher than a given threshold. We chose the threshold of 80, 90, and 95% of the maximum amplitude for each fault. The result of this analysis is shown in Fig. A3 in Electronic Supplement (faults in

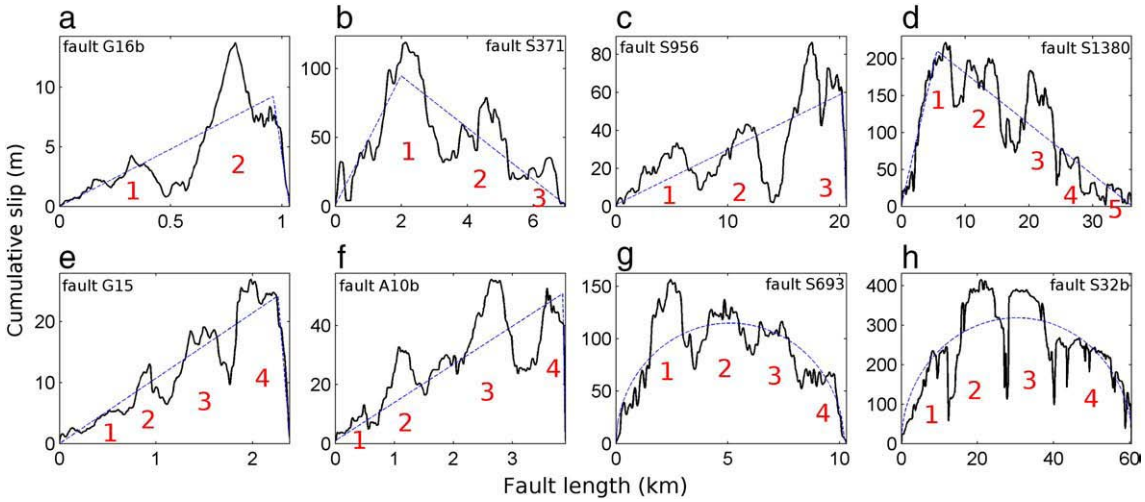

Fig. 4. Examples of analyzed fault slip profiles. Slip profiles in black. A and G in fault names are for faults located in Asal–Ghoubbet rift (A, onland; G, underwater), S for faults in central Afar (see Fig. 2). Faults have different lengths, maximum slips, ages and locations. Blue dotted curves are functions best fitting the slip profiles. Numbers in red indicate clearest major segments.

random order; see figure caption). Amplitudes higher than 80, 90, and 95% of the maximum value of each profile are reported in the plots a, b, and c, respectively. Plots d–e–f are derived from Fig. A3a–b–c respectively, and illustrate the number of cases having their largest energy amplitude (i.e., greater than 80, 90, and 95% of the maximum value, as before) at a given spatial frequency. Together the figures show that the vast majority of the slip profiles have their largest energy occurring over a narrow range of spatial frequencies, narrowing from 1–5 to 1–3 as the amplitude threshold is increased. Fig. 7a shows the distribution of the maximum amplitude of the frequency components as a function of the spatial frequency, for the entire population of the 927 profiles. It shows that the very large majority of the slip profiles (≈71%) contains major slip bumps that have a specific spatial frequency, hence a specific relative length scale. The number of major slip bumps ranges between 2 and 5 for 93% of the segmented faults, and is more commonly equal to only 2–4 (84% of the segmented faults). The 0 and 1 spatial frequencies indicate profiles for which the function f is either uniform or resembling a single sinusoid. Both thus reveal non-segmented slip profiles. This suggests that ≈29% of the faults have no significant segmentation or, said differently, are made of one single piece, hence one single segment. When triangular and elliptical slip profiles are distinguished (Fig. A4 in Electronic Supplement), it appears that the number of major segments may be slightly larger along faults having a triangular-shaped slip distribution (generally up to 4 [Fig. A4a], versus up to 3 on elliptical slip profiles [Fig. A4b]). When the fault lengths are discriminated as being shorter (Fig. A5a in Electronic Supplement) or longer (Fig. A5b) than the crustal thickness, the results described above remain unchanged: irrespective of their length, all faults have a limited, similar number of major segments, ranging between 2 and 4 for the majority of them, and more commonly equal to only 2 or 3.

3.3. S-transform analysis of the slip profiles

As shown on examples b, f and h in Fig. 4, the major slip bumps hence major segments along a fault may not have the exact same length. Though we did not observe it, some of them could also be isolated within a fault. For the reasons explained above, the Fourier spectrum analysis is not able to provide any information on such possible complexities. A more sophisticated method is thus required, that may allow describing the energy content of the signal in terms of both location and spatial frequency (i.e., size). The S-transform method is appropriate (Stockwell et al., 1996). It is a space–frequency spectral localization method combined with a wavelet-type analysis through a Gaussian window whose width scales inversely with the spatial frequency. The expression of the S-transform given by Stockwell et al. (1996) is:

$$S(\lambda,k)=\frac{1}{\sqrt{2\pi}}\int_{-\infty}^{\infty}s(x)\,|k|\,EXP\left[-\frac{(\lambda-x)^2k^2}{2}-i2\pi kx\right]\cdot dx$$

S denotes the S-transform of the signal $s(x)$ which is a function of space; k is the spatial frequency and λ is a parameter which controls the position in space of the Gaussian window. Note that the S-transform is not strictly a Continuous Wavelet Transform (CWT) but rather a hybrid between short time Fourier transform (STFT) and CWT. The signal is windowed with adaptative Gaussian functions of finite width which are localized in space. The S-transform thus allows the representation of the local spectrum. A simple averaging of those local spectra over space would give the Fourier spectrum used in Section 3.2. The frequency dependent resolution of the S-transform allows analyzing non-stationary fluctuations, as those observed in the slip profiles. Therefore in the following, we refer to the maximum value of $S(\lambda,k)$ at a given spatial frequency, to quantify the contribution of the length scale $1/k$.

Fig. 6 shows the results of the S-transform analysis conducted on the 8 example slip profiles. As before the analysis is performed on the fluctuating part of the slip signals (f; shown in Fig. 5). A zero-padding procedure is applied to the signals in order to analyze them with a broader range of Gaussian widths. The color spectra (middle plots) map the amplitude of the frequency components as a function of both the spatial frequency and the fault length. The histograms (bottom plots) report the maximum amplitude of the frequency components as a function of the spatial frequency. Together these figures show that, in all examples, the greatest signal energy occurs over a narrow range of spatial frequencies. In all cases, the dominant spatial frequencies range between 2 and 5. Most example profiles also contain higher frequencies hence smaller sizes oscillations. Yet the contribution of those high frequency oscillations to the signal shaping is far lower than that of the low frequency, major bumps. The results obtained on the examples thus show that the corresponding slip profiles contain oscillations of various sizes, yet are dominated by a first order of oscillations, which have a specific spatial frequency range hence a specific relative length scale. The numbers of first-order slip bumps that are derived from the dominant spatial frequencies are similar to the numbers of major slip bumps determined before from both visual observation and Fourier spectrum analysis.

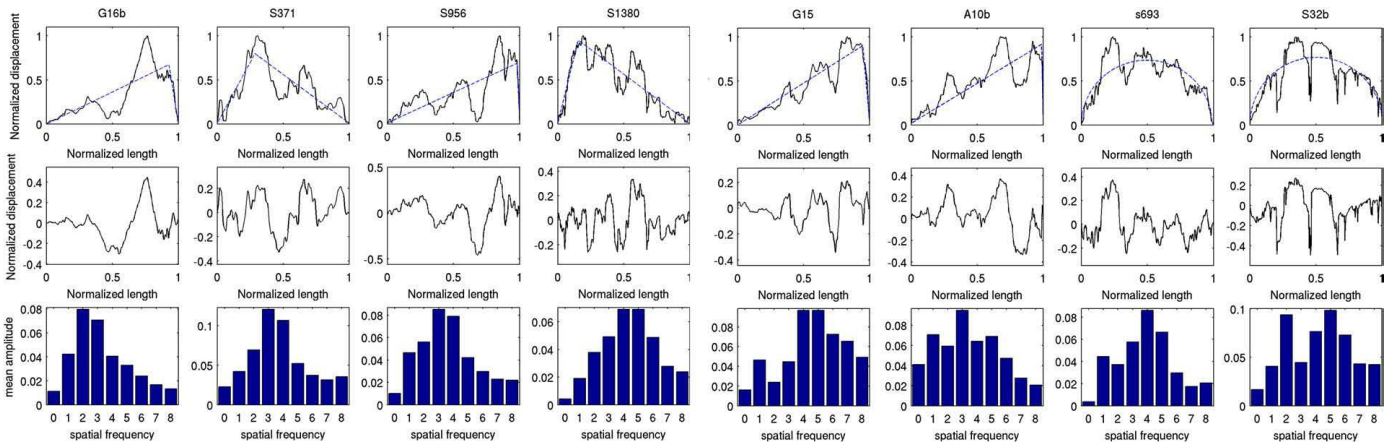

Fig. 5. Fourier spectrum analysis of the example slip profiles shown in Fig. 4. Top plots are the slip profiles normalized to their length and maximum slip (in black), and adjusted by the best-fitting function in blue. Medium plots are the residual slip functions derived from removing the envelope-functions (in blue above) from the slip profiles. Bottom plots report the mean amplitude of the frequency components as a function of the spatial frequency. See text for details.

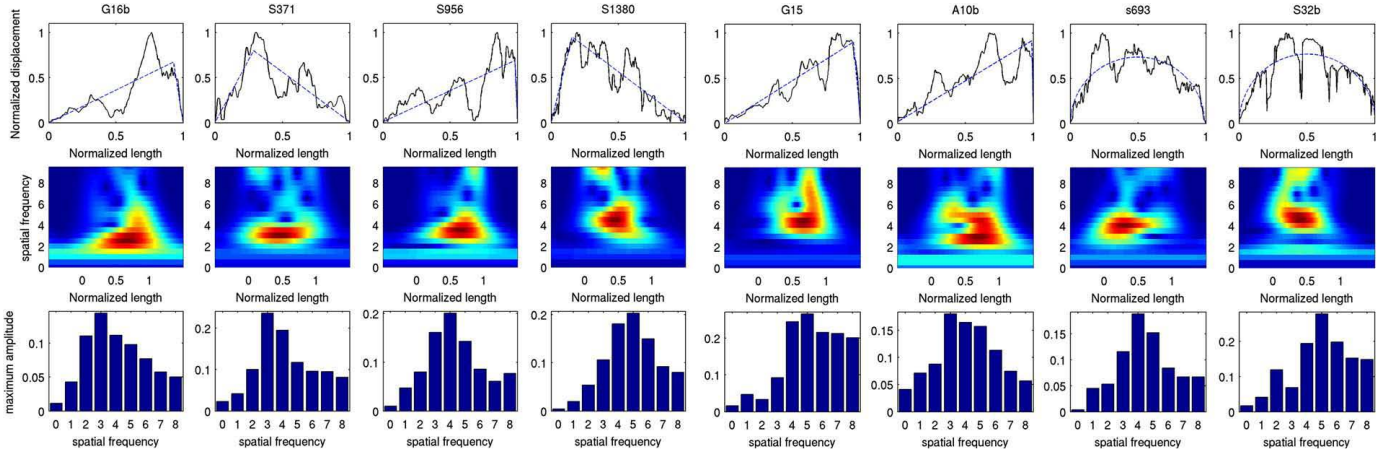

Fig. 6. S-transform analysis of the example slip profiles shown in Fig. 4. Top plots are the slip profiles normalized to their length and maximum slip (in black), and adjusted by the best-fitting function in blue. Medium plots map the amplitude of the frequency components as a function of both the spatial frequency and the fault length (higher amplitudes from blue to red). Bottom plots report the maximum amplitude of the frequency components as a function of the spatial frequency. See text for details.

Together these suggest that we may apply the S-transform analysis to the entire data set to recover the number and size of the major slip bumps within the slip-length profiles. Fig. A6 in Electronic Supplement presents the distribution of the dominant spatial frequencies for the entire fault population. To constrain the range of dominant frequencies, we have reported the distribution of the largest frequency component amplitudes as a function of the spatial frequency, for all profiles (random order; see figure caption). Amplitudes higher than 80, 90, and 95% of the maximum value for each profile are reported in the plots a, b, and c, respectively. Plots d–e–f are derived from Fig. A6a–b–c respectively, and illustrate the number of cases having their largest energy amplitude (i.e., greater than 80, 90, and 95% of the maximum value, as before) at a given spatial frequency. Because the importance of high frequencies is revealed in the plots, the histograms are extended up to frequencies of 20 to ensure the appropriate representation of the profiles energy content. Together the figures show that the slip profiles have their largest energy occurring over a broad range of spatial frequencies, commonly ranging between 2 and 10. Yet the importance of the high frequencies is a direct product of the S-transform method. The spectrum is indeed now local and no more averaged in space. As we consider the maximum of the S-transform for each frequency band, we are therefore more sensitive to local high frequencies associated with fluctuations in the slip profiles. As the threshold of the energy amplitude is increased, the profiles appear clearly dominated by low frequency major bumps, with the number of those bumps more generally ranging between 3 and 7. Fig. 7b shows the distribution of the maximum amplitude of the frequency components as a function of the spatial frequency, for the entire population of the 927 profiles. It shows that the very large majority of the slip profiles ($\approx$94%) contains slip bumps that have a specific spatial frequency, hence a specific relative length scale. The number of major slip bumps hence major segments ranges between 2 and 7 for the majority of the segmented faults ($\approx$70%; equivalent to $\approx$65% of the entire population), and is more commonly equal to only 3 to 5. The 0 and 1 spatial frequencies indicate profiles for which the misfit is either uniform or resembling a single Gaussian, hence reveal no segmentation. This suggests that $\approx$6% of the faults are not significantly segmented, or said differently, are made of a single major segment. Finally, the remaining $\approx$30% of the faults are found to contain a larger number (>7) of small-size segments. A visual inspection of those highly segmented profiles reveals however that, were those high frequencies ignored, the profiles would be concluded as not being segmented or, in many other cases, as including a few major segments (see examples in Section 3.4). This suggests that much more than 50% of the faults are segmented into 2 to 5 major segments, while more than 6% of the faults are un-segmented. When triangular and elliptical slip profiles are distinguished (Fig. A4c–d in Electronic Supplement), no clear difference is observed in the number of major segments, even though those are more clearly discriminated on triangular profiles (Fig. A4c). When the fault lengths are discriminated as being shorter or longer than the crustal thickness (Fig. A5c–d respectively in Electronic Supplement), the results described above remain unchanged: irrespective of their length, all faults have a limited, similar number of major segments, ranging between 2 and 5 for the majority of them. These findings are even more pronounced on short faults (Fig. A5c).

3.4. Limitations of the methods

As any signal-processing approach, the two methods that we use have both weak and strong sides. The weak side is that they may fail properly describing the characteristics of some individual slip profiles within the entire collection (see examples below). The strong side is that, when uniformly applied to a dense population as is the case here, they succeed in revealing robust, statistical properties of the slip profiles. The histograms in Fig. 7 (and A3 and A6) may contain a few misleading values, however their overall pattern is meaningful and defines average, common properties of the slip profiles. Additional

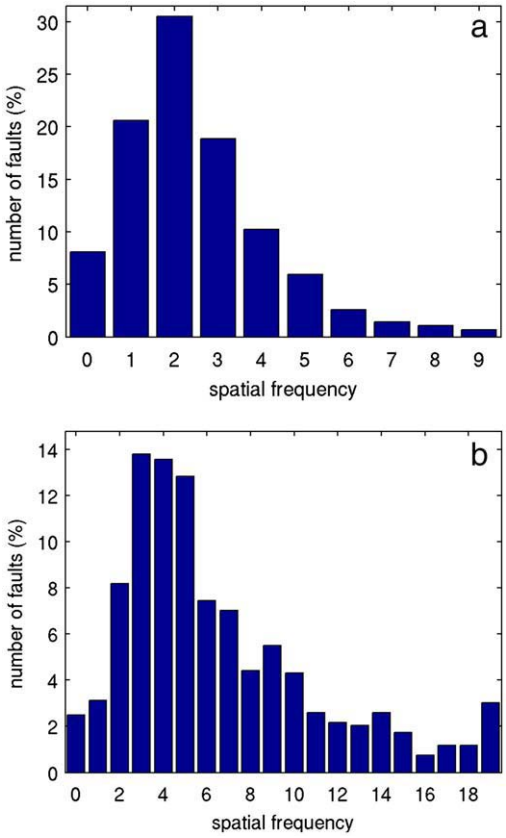

Fig. 7. Distribution of spatial frequencies at which the frequency components have a maximum amplitude, for the total fault population. a) Distribution derived from Fourier spectrum analysis. b) Distribution derived from S-transform analysis. The frequency range has been increased up to 19 to include the high frequency components. See text for details.

information is available through the S-transform as it provides insight into the location in space of the observed dominant frequencies. We therefore prefer it.

The major limitation of both methods, at least in the way we use them, is that they only allow revealing the slip fluctuations, hence the segments, which, on average, dominate the slip profiles (i.e., the 'highest' fluctuations). The Fourier spectrum reveals the average size of the largest segments, from which an average number of such segments is inferred. On the other hand, when using the S-transform, we reduce the rich, complex information contained in each individual space–frequency spectrum, to only two parameters — the maximum value and the spatial frequency at which it occurs. Thus, if the major segments within faults have different sizes, that variability is not fully revealed.

Another consequence is that, on profiles containing several orders of fluctuations, the results (from S-transform) may be biased toward the highest frequencies. Examples are shown in Fig. A7a in Electronic Supplement. Though the example slip profiles contain clear, large slip bumps, the S-transform method primarily reveals the higher frequency, smaller-scale oscillations. Thus, in such cases, the size and number of major segments is not properly revealed.

When the slip profiles do not contain any clear large segments (i.e., consist of a single major segment), the S-transform method generally finds a uniform or smooth residual, leading to properly emphasize the frequencies 0 or 1 (examples in Fig. A7b). Yet, in some other cases as those exemplified in Fig. A7c, the S-transform method preferentially catches the very high frequency components of the residuals, in effect masking the non-segmented property of the fault.

Finally, our approach does not provide any information on the 'amplitude' of the segmentation; as shown on the examples presented

in Fig. A7d, the number of recovered major segments is the same whether those segments are pronounced or more subtle features in the slip profiles.

4. Discussion and conclusions: implications for fault and earthquake mechanics

4.1. Major results and implications for long-term fault mechanics

Our analysis first confirms that most normal faults are segmented at a large-scale, i.e. are made of a number of large segments whose length is of the same order as that of their entire trace. Our work furthermore highlights two major properties of this large-scale segmentation. Firstly, we find that, irrespective of their length, the vast majority of the 927 faults have a similar number of major segments. Because the fault population that we have analyzed is both extremely dense and spanning a broad range of scales and ages, the above finding attests to a robust, general property of the faults which is that, irrespective of the scale, most faults contain the same number of major segments. This shows that the largest-scale segmentation of the faults analyzed here is self-similar. Secondly, our results show that the number of major segments is small, ranging between 2 and 5 for the majority of the faults (>50–70% of the total population, depending on the method), more commonly being between 3 and 5. The implication is that, irrespective of their scale, most faults are divided into only two to five major segments, and more commonly into three to five. That result is strikingly similar to that found by Otsuki and Dilov (2005) in their laboratory experiment aimed at investigating the geometrical evolution of experimental faults. Only few faults (10–30%) appear as not being significantly segmented, and are therefore made of one single major segment.

Though we have not analyzed the high frequency fluctuations of the slip profiles, a visual inspection of both the profiles and the S-transform spectra reveals that high frequency fluctuations, hence small-scale segments, exist in every fault. This indicates that not only are the faults divided into a few major segments, but those major segments are themselves divided into smaller-scale segments. The organization of that smaller-scale segmentation is not the scope of the paper, and will be the topic of further analysis. It is possible, as suggested by Otsuki and Dilov (2005) that, irrespective of the hierarchical ranks of the segmentation, the number of segments in any given hierarchical rank remains comprised between 2 and 5.

The self-similarity of the largest-scale segmentation of the faults means that the length of the major segments within faults is not similar from one fault to the other, but instead varies as a function of the total fault length. This point is highlighted in Fig. 8 which confirms that, in most cases, major segments within faults have a length which is twice to five times shorter than the total length of the fault they belong to. The length of the longest segments in faults is thus variable, here varying from a few hundred meters to 30–40 km (Fig. 8). This indicates that the largest-scale segmentation of the faults is not only dependent on the thickness and layering structure of the faulted medium, as has been commonly suggested (e.g., Sylvester, 1988; Scholz et al., 1991; Ouillon et al., 1996; Jackson, 2002; Klinger et al., 2006). The observation that faults that are shorter and longer than the crustal thickness show the self-similar property described above (Fig. A5) further confirms that the length of the major segments within faults is not only controlled by the seismogenic thickness. Our findings also contradict the hypothesis that the segmentation depends on preexisting heterogeneities of the crust or lithosphere, as suggested (e.g., Ouillon et al., 1996).

Fig. 9 shows that the number of major segments identified in the slip profiles decreases as a function of the slip to length ratio of the faults. In other words, faults having accumulated little slip appear more segmented than faults having slipped by large amounts. Slip profiles identified to not be segmented are actually those of the faults

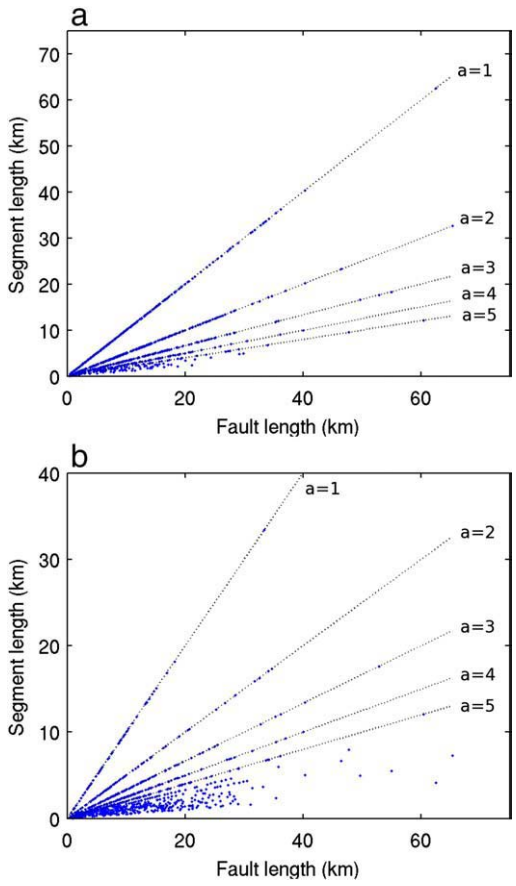

Fig. 8. Major segment length as a function of total fault length. a) Results are derived from Fourier spectrum analysis. b) Results are derived from S-transform analysis. Thin dotted lines show the relations most predominantly derived (for 94% of the fault population in a, and 55% in b).

having the largest D_{max}/L ratios, hence having accumulated the largest slips. This observation would correspond to a process where fault segments progressively connect as the fault accumulates slip, with the inter-segment slip troughs being progressively filled up and smoothed (e.g., Soliva and Benedicto, 2004). This shows that the number, hence also the size of the major segments within faults, vary over the fault evolution and are therefore at least partly controlled by the fault mechanics itself. The faults which appear as not being segmented (at large-scale) are in a mature state where their original major segments are fully linked and no more distinguishable in the fault slip profile. The observation of the segment number reduction with fault slip confirms that the complexity of the faults decreases with their maturity (Wesnousky, 1988; Stirling et al., 1996; Ben-Zion and Sammis, 2003; Manighetti et al., 2007).

Together the findings above suggest that the large-scale segmentation of the faults is at least partially dictated by the fault mechanics itself. This would imply that the results found here can be generalized to all faults, regardless of their scale and slip mode. This hypothesis is confirmed by most available maps of surface traces of strike-slip, reverse and normal faults worldwide, showing those traces divided into a few major segments only (e.g., Stirling et al., 1996; Wesnousky, 2006; Fig. A8 in Electronic Supplement).

Why the number of major segments along faults remains within the same narrow range over the fault evolution is a key question that deserves further study. The data analyzed here cannot alone solve this question. Yet, if as suggested by Schlagenhauf et al. (2008), the long-term growth of faults occurs through alternating phases of slip accumulation at constant length and lateral propagation with little slip increase, then one may suggest that the static stress concentration

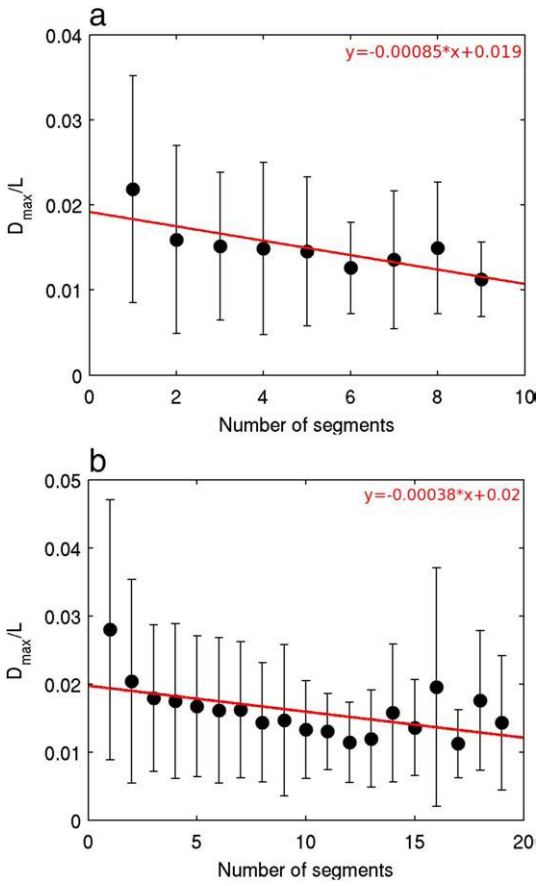

Fig. 9. Slip to length ratio of faults as a function of number of major segments. a) Results are derived from Fourier spectrum analysis. b) Results are derived from S-transform analysis. In both plots, vertical lines show the standard deviation of the slip-length ratios, while solid dots are averaged values. The regression (red) is calculated from averaged values.

which builds up around the fault tips during slip accumulation at constant length likely plays a role in the formation of segments ahead of the fault tips. Depending on the ratio between those near-tip stress concentrations and the strength of the medium at the fault tips, one or two major segments may eventually form at one or both tips of a growing fault, respectively. It is likely that the length of such newly formed segments would depend on the level of the near-tip stress concentration, which, in turn, depends on the length of the growing fault. Once segments are formed at the tip of a growing fault, the latter may propagate laterally by connecting to those segments. This process would result in a longer fault, now made of two or three major segments, and ready to resume accumulating slip at such a new, greater constant length. The process would then repeat as before. We suggest that, though it is only qualitative and lacking solid constrains, this conceptual vision of the long-term evolution of the faults may provide a framework to understand the self-similarity of the large-scale segmentation of faults.

4.2. Implications for earthquake behavior

The faults that we have analyzed have ages ranging between approximately 10^4 and 10^6 yr. They therefore have a long history of slip, and their cumulative slip profiles are the direct products of this long history. Though we ignore when the major segments presently observed in the slip profiles initially formed, it is clear that they have been shaping the slip profiles for a long time, encompassing hundreds to thousands of seismic cycles; smoothing the large slip deficits (several tens to hundreds of meters high; see Fig. 4) at the major inter-segments indeed requires a long slip history (as the slip rates are 0.5–5 mm/yr). The major segments and inter-segments that markedly shape the slip profiles are thus long-lived features. This property of the large-scale segments within faults has been recognized in a number of previous studies. On the other hand, because they are the longest within a fault, the major segments we are dealing with are likely to be 3D features, effectively dividing the fault entirely from its top (i.e., the surface) to bottom, i.e. the complete seismogenic zone for large faults (e.g., Segall and Pollard, 1980). Hence the large-scale segments and inter-segments within faults are long-lived, 3D features which are expected to have an important impact on the earthquakes which break those faults.

The key ingredient of the fault segmentation impact on the earthquakes is likely to arise from the specific mechanical and rheological behavior of the major inter-segments. Major segments within faults terminate through high slip gradients (see Fig. 4), so that extremely high strain concentrations are expected in the inter-segment zones. Yet, those inter-segments are zones of persisting, large slip deficit. That is, despite of the very high strain concentrations which they sustain, the inter-segment zones do not or hardly slip, hence, obviously, do not respond as expected if elastic stresses build up during the repeated seismic cycles. It is well established that the inter-segment zones are regions of distributed and pervasive small-scale cracking and faulting, commonly described as damage (e.g., King 1983; Sibson, 2003; Manighetti et al., 2004). Such pervasive damage is likely to markedly modify the rheology of the crust in the major inter-segments zones, allowing it to accommodate the high stresses and strains in a manner close to plasticity. The major inter-segment zones would thus be 'soft or weak barriers' as defined by Manighetti et al. (2004), capable to diffuse high stresses and strain, hence prevent elastic storage and breakage. As such, they would be efficient barriers to earthquake rupture propagation (e.g., Aki, 1979; Barka and Kandisky-Cade, 1988; Manighetti et al., 2001a, 2004, 2005; Shaw, 2006). The plastic versus elastic behavior of the inter-segment zones seems however to evolve in time, as the number of distinguishable major segments along a fault decreases with its slip to length ratio. This behavior must arise from the slip deficits in the inter-segment zones decreasing as the fault overall accumulates more slip. As a fault accumulates more slip hence becomes more mature, the mechanical behavior of its major inter-segment zones would therefore evolve from being dominated by plasticity to becoming more fragile. This scenario remains to be modeled.

The self-similarity of the large-scale segmentation of the faults indicates that, irrespective of their size, most faults contain 1 to 4 zones along their length — the major inter-segments — which are prone to stop an earthquake rupture. The capacity of those zones to arrest a rupture depends on their rheological behavior, which in turn depends on the structural maturity of the fault they belong to. An earthquake rupture that initiates on an immature fault, i.e. a fault having a short slip history and a small amount of slip per unit of length, would generally die out at the first significant 'plastic spot' encountered along its course. Its dynamic stress could trigger the rupture of a neighboring segment however, but this segment would then break as an independent patch. In such a case, the successive breaking of 2 or more major segments along the fault would result in a final displacement–length ratio being apparently low, though the stress drop on each broken segment may be high. By contrast, an earthquake rupture that initiates on a more mature fault would propagate along a more homogeneous medium, primarily responding elastically to the stress load. The rupture would thus more easily break in continuity several or all of the 2 to 5 major segments that constitute the fault. This breaking would produce a unique slip patch along the fault, with a final displacement–length ratio directly related to the stress drop on the entire fault. That idea has been recently put forward by Manighetti et al. (2007), and shown to successfully account for the large variability observed in the available displacement–length data of continental earthquakes.

Finally, the finding that the faults are punctuated by a few major inter-segments whose barrier effect to slip propagation can persist over hundreds to thousands of seismic cycles, provides an evidence for the existence of 'characteristic' earthquakes or earthquake sequences (Schwartz and Coppersmith, 1984), restrained to break the exact same portion(s) of the faults over very long time periods. In such characteristic earthquakes or sequences, only the total rupture length is characteristic however, while the other earthquake parameters, such as the slip, may be variable.

To conclude, our work provides two major results: Firstly, we have shown that the largest-scale segmentation of the faults is self-similar, that is faults have the same number (typically, 2–5) of major segments independent of their length, age and slip rate. It is likely that such a self-similar property derives from the mechanics of faulting, even though the question is open as to the mechanical/physical ingredients that are needed in fault models to make them capable to reproduce such a behavior. Secondly, the above finding implies that, whatever the fault on which they initiate, large earthquakes face the same number of major segments to potentially break. Yet the number of segments eventually broken by the known earthquakes clearly differs from one case to another. These differences will also need to be addressed in the fault and earthquake models. We suggest that this variability is intimately related to the fault history; the number of major segments ruptured during a large earthquake would depend on the connection state of the segments, hence on the slip history, or structural maturity, of the fault.

Appendix A. Supplementary data

Supplementary data associated with this article can be found, in the online version, at doi:10.1016/j.epsl.2009.09.040.

References

Aki, K., 1979. J. Geophys. Res. 84, 6140–6148.
Audin, L., Manighetti, I., Tapponnier, P., Métivier, F., Jacques, E., 2001. Geophys. J. Int. 144, 1–28.
Aviles, C.A., Scholz, C.H., 1987. J. Geophys. Res. 92, 331–344.
Aydin, A., Schultz, R.A., 1990. J. Struct. Geol. 12, 123–129.
Barka, A.A., Kandisky-Cade, K., 1988. Tectonics 7, 663–684.
Ben-Zion, Y., Sammis, C.G., 2003. Pure Appl. Geophys. 160, 677–715.
Brown, S., Scholz, C.H., 1985. J. Geophys. Res. 90, 12575–12582.
Das, S., 2003. Pure Appl. Geophys. 160, 579–602.
Davis, K., Burbank, D.W., Fisher, D., Wallace, S., Nobes, D., 2005. J. Struct. Geol. 27, 1528–1546.
De Chabalier, J., Avouac, J., 1994. Science 265, 1677–1681.
DePolo, C.M., Clark, D.G., Slemmons, D.B., Ramelli, A.R., 1991. J. Struct. Geol. 13, 123–136.
Doubre, C., Manighetti, I., Dorbath, C., Dorbath, L., Jacques, E., Delmond, J.C., 2007a. J. Geophys. Res. 112. doi:10.1029/2005JB003940.
Doubre, C., Manighetti, I., Dorbath, L., Dorbath, C., Bertil, D., Delmond, J.C., 2007b. J. Geophys. Res. 112. doi:10.1029/2006JB004333.
Ellis, M.A., Dunlap, W.J., 1988. J. Struct. Geol. 10, 183–192.
Ferrill, D.A., Stamatakos, J.A., Sims, D., 1999. J. Struct. Geol. 21, 1027–1038.
Harris, R.A., Day, S.M., 1993. J. Geophys. Res. 98, 4461–4472.
Harris, R.A., Day, S.M., 1999. Geophys. Res. Lett. 26, 2089–2092.
Jackson, J.A., 2002. International Handbook of Earthquake and Engineering Seismology, p. 81A.
Kagan, Y.Y., 1994. Physica 77, 160–192.
King, G.C.P., 1983. Pure Appl. Geophys. 121, 761–815.
King, G., Nabelek, J., 1985. Science 228, 984–987.
Klinger, Y., Michel, R., King, G.C.P., 2006. Earth Planet. Sci. Lett. 242, 354–364.
Lettis, W., Bachhuber, J., Witter, R., Brankman, C., Randolph, C.E., Barka, A., Page, W.D., Kaya, A., 2002. Bull. Seismol. Soc. Am. 92, 19–42.
Li, Y.G., Aki, K., Adams, D., Hasemi, A., Lee, W.H.K., 1994. J. Geophys. Res. 99, 11705–11722.
Machette, M.N., Personius, S.F., Nelson, A.R., Schwartz, D.P., Lund, W.R., 1991. J. Struct. Geol. 13, 137–150.
Manighetti, I., Tapponnier, P., Courtillot, V., Gruszow, S., Gillot, P.Y., 1997. J. Geophys. Res. 102, 2681–2710.
Manighetti, I., Tapponnier, P., Gillot, P.Y., Jacques, E., Courtillot, V., Armijo, R., Ruegg, J.C., King, G., 1998. J. Geophys. Res. 103, 4947–4974.
Manighetti, I., King, G., Gaudemer, Y., Scholz, C.H., Doubre, C., 2001a. J. Geophys. Res. 106, 13667–13696.
Manighetti, I., Tapponnier, P., Courtillot, V., Gallet, Y., Jacques, E., Gillot, P.Y., 2001b. J. Geophys. Res. 106, 13613–13665.
Manighetti, I., King, G., Charles, G., Sammis, G., 2004. Earth Planet. Sci. Lett. 217, 399–408.
Manighetti, I., Campillo, M., Sammis, C., Mai, M., King, G., 2005. J. Geophys. Res. 110. doi:10.1029/2004JB003174.
Manighetti, I., Campillo, M., Bouley, S., Cotton, F., 2007. Earth Planet. Sci. Lett. 253, 429–438.
Nicol, A., Walsh, J., Berryman, K., Nodder, S., 2005. J. Struct. Geol. 27, 327–342.
Okubo, P.G., Aki, K., 1987. J. Geophys. Res. 92, 345–356.
Otsuki, K., Dilov, T., 2005. J. Geophys. Res. 110. doi:10.1029/2004JB003359.
Ouillon, G., Castaing, C., Sornette, D., 1996. J. Geophys. Res. 101, 5477–5787.
Peacock, D.C.P., 1991. J. Struct. Geol. 13, 1025–1035.
Peacock, D.C.P., Sanderson, D.J., 1991. J. Struct. Geol. 13, 721–733.
Power, W.L., Tullis, T.E., Brown, S.R., Boitnott, G.N., Scholz, C.H., 1987. Geophys. Res. Lett. 14, 29–32.
Schlagenhauf, A., Manighetti, I., Malavieille, J., Dominguez, S., 2008. Earth Planet. Sci. Lett. 273, 299–311.
Scholz, C., 2002. The Mechanics of Earthquakes and Faulting, second ed. Cambridge University Press.
Scholz, C., Riste, T., Sherrington, D., 1991. eds. 41.
Schwartz, D.P., Coppersmith, K.J., 1984. J. Geophys. Res. 89, 5681–5698.
Segall, P., Pollard, D.D., 1980. J. Geophys. Res. 85, 4337–4350.
Shaw, B.E., 2006. J. Geophys. Res. 111. doi:10.1029/2005JB004093.
Shaw, B.E., Dieterich, J.H., 2007. Geophys. Res. Lett. 34. doi:10.1029/2006GL027980.
Sibson, R.H., 1985. Nature 316, 248–251.
Sibson, R.H., 1986. Annu. Rev. Earth Planet Sci. 14, 149–175.
Sibson, R.H., 2003. Bull. Seismol. Soc. Am. 93, 1169–1178.
Simpson, R.W., Barall, M., Langbein, J., Murray, J.R., Rymer, M.J., 2006. Bull. Seismol. Soc. Am. 96. doi:10.1785/0120050824.
Soliva, R., Benedicto, A., 2004. J. Struct. Geol. 26, 2251–2267.
Stein, R.S., Briole, P., Ruegg, J.C., Tapponnier, P., Gasse, F., 1991. J. Geophys. Res. 96, 21,789–21,806.
Stirling, M., Wesnousky, S.G., Shimazaki, K., 1996. Geophys. J. Int. 124, 833–868.
Stockwell, R.G., Mansinha, L., Lowe, R.P., 1996. IEEE Trans. Signal Process. 44, 998–1001.
Sylvester, A.G., 1988. Geol. Soc. Am. Bull. 100, 1666–1703.
Tchalenko, J.S., Berberian, M., 1975. GSA Bull. 86, 703–709.
Walsh, J.J., Bailey, W.R., Childs, C., Nicol, A., Bonson, C.G., 2003. J. Struct. Geol. 25, 1251–1262.
Wesnousky, S.G., 1988. Nature 335, 340–343.
Wesnousky, S., 2006. Nature 444, 358–360.
Wesnousky, S.G., 2008. Bull. Seismol. Soc. Am. 98. doi:10.1785/0120070111.
Zhang, P., Slemmons, D.B., Mao, F., 1991. J. Struct. Geol. 13, 165–176.
Zhang, P., Mao, F., Slemmons, D.B., 1999. Tectonophysics 308, 37–52.